ELSEVIER

Ultramicroscopy 69 (1997) 279–287

ultramicroscopy

Electronic contribution to secondary electron compositional contrast in the scanning electron microscope

Martin R. Castell[a,*,1], Doug D. Perovic[a], Hugues Lafontaine[b]

[a] Department of Metallurgy and Materials Science, University of Toronto, Toronto, Canada M5S 3E4

[b] Institute for Microstructural Sciences, National Research Council, Ottawa, Canada K1A 0R6

Received 18 February 1997; received in revised form 16 June 1997

Abstract

Scanning electron microscopy of cleavage surfaces through a variable thickness Si–$Ge_{0.25}Si_{0.75}$ heterostructure is shown to reveal the high sensitivity of the secondary electron signal to small changes in band structure. $Ge_{0.25}Si_{0.75}$ layers that are coherently strained appear brighter in secondary electron micrographs than equal thickness layers of the unstrained $Ge_{0.25}Si_{0.75}$ alloy. This effect has been studied quantitatively and is explained in terms of the 0.1 eV strain-induced raising of the $Ge_{0.25}Si_{0.75}$ valence band edge resulting in an increased secondary electron escape probability.

PACS: 61.16.Bg; 71.20.Mq

Keywords: Secondary electron; Scanning electron microscopy; Strain; Heterostructure

1. Introduction

Over the last two decades there have been significant advances in the electron optics and detector designs of scanning electron microscopes (SEMs) that now allow these instruments to operate at a level where they can be routinely used to evaluate materials with nanometre-scale structures. A good example of this is the imaging of semiconductor multiple quantum well heterostructures by secondary electrons (SE) and backscattered electrons (BSE) [1–9]. Compositional contrast arising between different materials as in the case of GaAs–$Al_xGa_{1-x}As$ and Si–Ge_xSi_{1-x} heterostructures are well documented, and the SE and BSE contrast has been explained in terms of differences in stopping power and atomic number.

The realization that n- and p-doped regions can be readily distinguished from intrinsic material in SE images [5, 8, 10–14] has recently received much attention and reveals the high sensitivity of the SE signal to small differences in the local electronic environment, which in the dopant contrast case is

* Corresponding author.

[1] On leave from Department of Materials, University of Oxford, Parks Road, Oxford OX1 3PH, UK.

0304-3991/97/$17.00 © 1997 Elsevier Science B.V. All rights reserved
PII S0304-3991(97)00051-X

caused by surface band bending [5, 8, 13]. Alternatively, changes in local band structure can also be achieved through the introduction of a deformation potential associated with elastically strained epitaxial layers. For example, if Ge_xSi_{1-x} layers are grown epitaxially on a Si substrate the indirect band gap of a coherently strained Ge_xSi_{1-x} layer is smaller than the unstrained alloy of the same composition [15, 16]. For the case of a $Ge_{0.25}Si_{0.75}$ layer on a Si substrate the reduction in the band gap from the unstrained to the strained case is approximately 0.1 eV where this reduction is mainly due to a raised valence band edge of the strained layer [17].

A Ge_xSi_{1-x} layer grown epitaxially on a Si substrate will initially grow pseudomorphically and be coherently strained. As the layer thickness increases, a point is reached where the elastic strain energy accumulated in the layer becomes larger than the energy associated with either (i) the introduction of strain-relieving misfit dislocations at the Ge_xSi_{1-x} interface or (ii) a morphological surface instability giving rise to surface waves/cusps [18]. In either case the strained layer possesses a *critical* thickness above which one of the competing relaxation mechanisms will partially or completely relax the layer towards its free-standing lattice constant. In practice, metastable layers above the equilibrium critical thickness can be grown such that a kinetic critical thickness exists which is determined by composition, growth rate and growth temperature [18].

In this paper we present quantitative SE signal measurements on a Si–$Ge_{0.25}Si_{0.75}$ heterostructure that contains thin, strained $Ge_{0.25}Si_{0.75}$ layers and thicker, relaxed $Ge_{0.25}Si_{0.75}$ layers. This sample allows us to measure the changes in SE signal due to the strain-induced valence band shift.

2. Experimental procedures

The Si–$Ge_{0.25}Si_{0.75}$ heterostructure used in the experiments was grown epitaxially on a (001)-oriented Si substrate at 525°C by ultra-high vacuum chemical vapour deposition (UHV-CVD). Details of the growth conditions and apparatus are described by Lafontaine et al. [19]. Twelve $Ge_{0.25}Si_{0.75}$ layers were grown with thicknesses increasing from 1 to 100 nm, separated by 50 nm layers of Si. Compositional uniformity of the $Ge_{0.25}Si_{0.75}$ layers typically has a maximum variation of $\pm 0.15\%$ across the wafer. For the growth conditions employed here, metastable $Ge_{0.25}Si_{0.75}$ layers thicker than ~ 25 nm will relax the elastic strain imposed by the Si substrate, firstly by misfit dislocation formation followed by surface wave formation [18].

A rapid thermal anneal was performed on the as-grown Si–$Ge_{0.25}Si_{0.75}$ heterostructure at 850°C for 30 s. This process causes metastable $Ge_{0.25}Si_{0.75}$ layers exceeding the equilibrium critical thickness to relax the built-in elastic strains without incurring significant interdiffusion between the layers; the equilibrium critical thickness of $Ge_{0.25}Si_{0.75}$ layers is a few nanometres [18, 19]. The dislocation structures of thin foils prepared by ion-beam milling of the as-grown and annealed samples were studied in a Hitachi H-800 transmission electron microscope (TEM) at 200 keV.

For SEM investigation cross-sectional cleavage was performed in air and the sample was immediately clipped into a specimen holder and introduced into the vacuum chamber of a Hitachi S4500II SEM. This SEM is equipped with a field emission (FE) electron source and was operated using the minimum accessible working distance of 3 mm. The energy of the primary electrons where the observations described in this paper were most clearly seen, were 1 keV for SE imaging and 20 keV for BSE imaging. All SEM images were digitally recorded as 1024×768 pixels with 256 grey-scales per pixel. Image analysis was performed using the NIH Image software package (version 1.59).

3. Results and discussion

A SE image of a cross-section through the as-grown variable thickness Si–$Ge_{0.25}Si_{0.75}$ heterostructure is shown in Fig. 1a. The bright regions are $Ge_{0.25}Si_{0.75}$ layers separated by darker 50 nm Si layers. As the micrographs are recorded electronically it is possible to use image-analysis software to integrate the SE signal intensities along lines parallel to the $Ge_{0.25}Si_{0.75}$ layers. The result of this

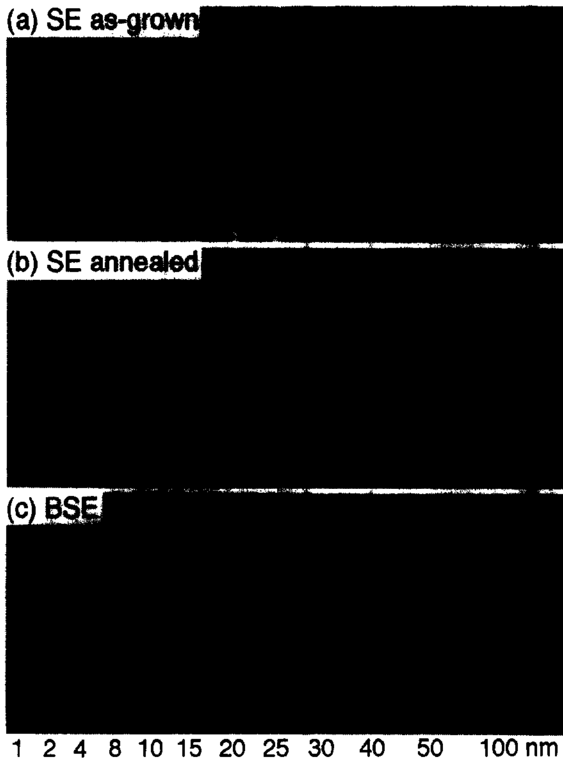

Fig. 1. Secondary electron images from the as-grown (a) and annealed (b) samples, aligned with a backscattered electron image (c) of a cleaved cross-section through the variable thickness Si–$Ge_{0.25}Si_{0.75}$ heterostructure. The $Ge_{0.25}Si_{0.75}$ layers (thicknesses indicated in nanometres) appear bright relative to the 50 nm thick Si spacer layers. In the SE image (a) the thin $Ge_{0.25}Si_{0.75}$ layers up to the 25 nm layer appear brighter than the thicker layers. This cannot be seen in the case of the SE annealed sample (b) or in the BSE image (c) where the layer brightness increases steadily with increasing layer thickness. SE images (a) and (b) were taken at 1 keV, and the BSE image (c) was taken at 20 keV.

integration gives an average SE intensity profile perpendicular to the layers. Profiles of this type show the variation of the SE signal due to the $Ge_{0.25}Si_{0.75}$ layers but there is also a varying background level that requires subtraction. This is achieved by fitting a curve through the minima of the profile and subtracting the curve from the raw data. In practice, the variation of the background is usually less than 8% contrast across a 1 μm scan region.

In order to quantitatively compare different profiles, all data has been presented in absolute contrast units. Contrast can only be calculated if the unsaturated zero signal level for each profile is known and is defined as

$$\text{Contrast} = \frac{SE_{\text{signal}} - SE_{\text{background}}}{SE_{\text{background}}}.$$

Here the SE background level (equivalent to 0% contrast) is the intensity of the 50 nm Si spacer layers relative to the SE zero level. A SE contrast profile of Fig. 1a with background subtracted is shown in Fig. 2a. The contrast of the $Ge_{0.25}Si_{0.75}$ layers initially increase with increasing thickness but beyond the 25 nm layer there is a sudden drop in intensity for the 30 nm layer followed by a gentle increase in intensity (with smaller slope) up to the 100 nm layer located at the sample edge. Fig. 2b and Fig. 2c show similar SE contrast profiles from other regions of the sample. The notable feature here is that in Fig. 2b it is the 20 nm layer that appears brightest and beyond which the SE contrast drops drastically. In Fig. 2c the same is true for the 15 nm layer. It should also be noted that of the 54 profiles examined from various parts of the as-grown sample either the 15 nm, 20 nm or 25 nm appeared brightest and all layers thicker than the brightest layer were significantly less intense. Irregularities in the SE yield caused by steps on the cleavage face were also observed on the samples. Bright lines due to steps have a characteristic signature, and it is not difficult to distinguish this type of increase in SE yield from that caused by the $Ge_{0.25}Si_{0.75}$ layers. Any images containing features due to steps were not included in the analysis.

From the profiles Fig. 2a–Fig. 2c of the as-grown sample it is apparent that there may be a correlation between strain in the $Ge_{0.25}Si_{0.75}$ layers and enhanced SE emission as suggested previously [5]. To provide further evidence of this relationship, we obtained SE images of the annealed Si–$Ge_{0.25}Si_{0.75}$ heterostructure where the critical layer thickness is only a few nanometres as described above [18, 19]. The sample was annealed and then cleaved to reveal a cross-section through the heterostructure. A SE image of the annealed sample is shown in Fig. 1b and the equivalent profile is in Fig. 2d. From this profile it is immediately apparent that the thin $Ge_{0.25}Si_{0.75}$ layers no longer

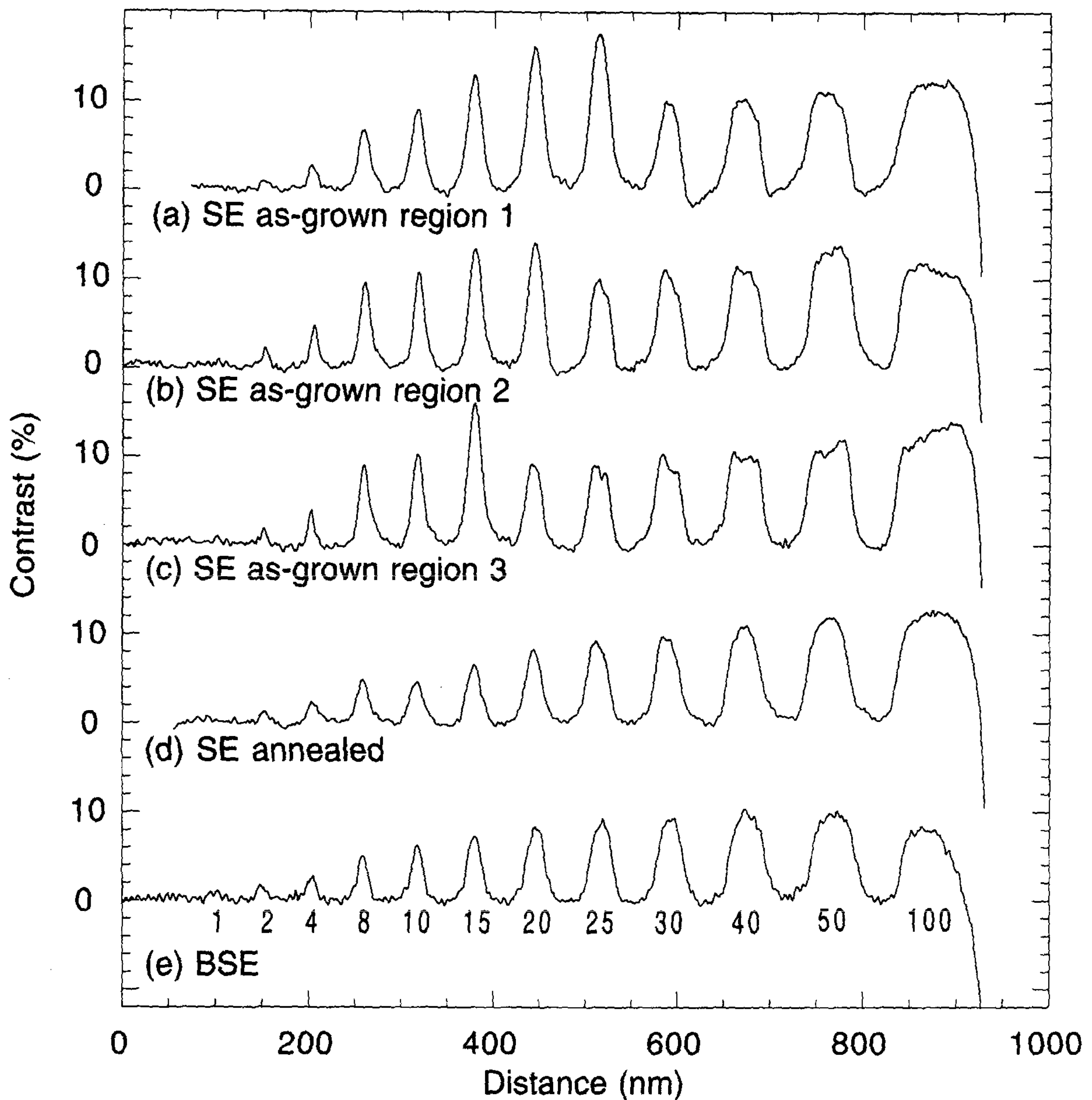

Fig. 2. Contrast profiles from images of the Si–$Ge_{0.25}Si_{0.75}$ heterostructure. Secondary electron profiles (a–c) taken at 1 keV from various parts of the as-grown sample show how it can be either the 25 nm (a), 20 nm (b), or 15 nm (c) $Ge_{0.25}Si_{0.75}$ layer that appears brightest. The profiles in (a), (d) and (e) were generated from images in Fig. 1a–Fig. 1c, respectively. Annealing at 850°C for 30 s causes the metastable layers to relax and they no longer show enhanced brightness in the SE profile (d). The BSE profile (e), taken at 20 keV, shows continuously increasing brightness with $Ge_{0.25}Si_{0.75}$ layer thickness as indicated in nanometres. BSE profiles of the as-grown and annealed samples, and from various parts of the samples, are indistinguishable within the noise limit.

show enhanced brightness compared with the as-grown sample. In Fig. 2d the 8 nm layer has a slightly higher intensity than the 10 nm layer which may indicate that the 8 nm layer is partially strained, but the 8 nm layer is certainly not fully strained because the SE intensities of the 8 nm layers from the as-grown sample are about twice as high.

To confirm that the as-grown sample contained metastable strained $Ge_{0.25}Si_{0.75}$ layers up to 25 nm, and that the annealed sample contained virtually no strained layers, cross-sectional thin specimens were prepared and investigated by TEM. Fig. 3a is a cross-sectional image of the 12-layer heterostructure taken using diffraction conditions that highlight the layer contrast without revealing dislocation structure. Fig. 3b is a diffraction contrast image showing a region of the specimen where one variant of the orthogonal misfit dislocation array is observed. The short interfacial dislocation segments are perpendicular to the $\langle 1\,1\,0 \rangle$ cross-sectional surface and are revealed by the characteristic oscillatory contrast following specimen tilting. It was found that a significant 60° misfit dislocation density was associated with layers 25 nm or greater in thickness. Some areas of the sample revealed misfit dislocation segments at the 20 nm layers but the densities were low on the cross-sectional TEM scale. It is interesting to note that the thickest layer (100 nm) has also exceeded the critical thickness for surface-wave relaxation of the misfit strain as seen in Fig. 3a.

Following rapid thermal annealing of the structure shown in Fig. 3a and Fig. 3b, a much higher misfit dislocation density was observed as shown in Fig. 3c where both $\langle 1\,1\,0 \rangle$ dislocation line variants are revealed. In this case, $Ge_{0.25}Si_{0.75}$ layers as thin as 10 nm have relaxed by dislocation formation. Moreover, misfit dislocations have also been generated at the base of the 12-layer heterostructure (i.e. at the 1 nm layer interface) since this is an energetically favourable condition for relaxation of the complete multilayer stack [20].

To rule out any variation of Ge concentration in the $Ge_{0.25}Si_{0.75}$ layers, which could be responsible for the enhanced SE contrast in the thinner layers in the as-grown sample, we obtained BSE images of the same regions, as shown in Fig. 1c. The BSE contrast profile of Fig. 1c is shown in Fig. 2e and was processed in the same way as the SE profiles. Fig. 2e is representative of all BSE profiles that were examined from both the as-grown and annealed samples with insignificant variations between profiles from different parts of the samples. The BSE signal contrast increases steadily with increasing $Ge_{0.25}Si_{0.75}$ layer thickness as expected from a sample of this type [2]. The $Ge_{0.25}Si_{0.75}$ layers appear bright relative to the Si layers because of their higher average atomic number. The backscattering coefficient η has been found to increase monotonically with increasing atomic number [21] and experimentally determined values at 20 keV are $\eta_{Si} = 0.194$ and $\eta_{Ge} = 0.332$ [22]. One would therefore expect the contrast level between bulk Si and bulk $Ge_{0.25}Si_{0.75}$ to be around 18%; however, even for the thickest $Ge_{0.25}Si_{0.75}$ layers in Fig. 2e the contrast only reaches approximately 10%. This is because the contrast in this profile is only caused by high-angle scattered BSEs rather than all the BSEs, which in turn is why the resolution far exceeds the 4.7 μm Bethe electron range for Si at 20 keV. The reason why the thicker layers appear brighter although they have the same Ge content as the thinner layers is that when the electron beam is located in the centre of a thin layer only a small fraction of the high-angle scattered BSEs that reach the detector were, in fact, scattered by the $Ge_{0.25}Si_{0.75}$ layer and most were scattered by the surrounding Si. As the layer thickness increases, more of the detected BSEs are scattered by the $Ge_{0.25}Si_{0.75}$ layer which as a stronger scatterer than the surrounding Si causes the thicker layers to appear brighter. This phenomenon has been discussed extensively by Merli and Nacucchi [2], and Konkol et al. [23]. These authors also show that for a given primary beam energy there will be a certain layer width that shows enhanced BSE contrast. Our layer widths are not large enough to observe this effect with 20 keV primary electrons, but it is conceivable that the 1 keV SE images might include this effect due to SE2 generation [21]. This would result in enhanced contrast of the layers around 10 nm, but we do not see this, probably because other SE contrast mechanisms dominate at low accelerating voltages.

The complete lack of abrupt variations in the Ge content of the $Ge_{0.25}Si_{0.75}$ layers rules out this

scenario as being responsible for the behaviour of the as-grown SE profiles of Fig. 2a–Fig. 2c and further strengthens the argument that the increased SE emission can be correlated with strain in the layers. As mentioned in the introduction, an elastically strained $Ge_{0.25}Si_{0.75}$ layer will have a valence band edge that is approximately 0.1 eV higher than the unstrained alloy and we argue that it is this offset that causes the increase in SE emission of the strained layers. Fig. 4 is a schematic diagram that shows the alignments of the valence and conduction bands for unstrained and coherently strained $Ge_{0.25}Si_{0.75}$ layers sandwiched between unstrained Si layers. As indicated, the strained alloy layer has a valence band edge that lies 0.1 eV closer to the vacuum level than when it is unstrained.

Total SE emission is determined by SE production, SE migration from the point of excitation to the surface, and escape of the SE over the surface potential barrier. The energy required to raise an electron from the Fermi level to a state of rest outside the surface (the vacuum level) is called the work function. For metals, the relationship between the work function and the minimum amount of energy an electron in the solid requires to contribute to SE emission is unambiguous because of the high electron population and high density of states at the Fermi level of a metal. For semiconductors, the work function represents the weighted average of the energies necessary to remove an electron from the valence and conduction bands. However, the population of electrons in the conduction band is insufficient to cause a significant contribution to the SE signal. Therefore, in a semiconductor the most relevant value for SE emission is the energy difference between the highly populated valence band and the vacuum level, and is referred to as the ionization potential of a solid. In fact, the situation is not always quite that straightforward due to pinning of the Fermi level by the high density of surface-gap states, as is the case with Si. A band of surface states is located approximately in the middle of the gap and is half filled, as shown in Fig. 4. Excitation of SEs from these surface states will also contribute to the total SE signal. Both the work function and the ionization potential will be reduced in the compressively strained $Ge_{0.25}Si_{0.75}$ layers compared with the unstrained alloy. For unstrained Si the ionization potential is around 5.3 eV and the work function is 4.8 eV depending on the crystal face and surface condition. The exact size of the ionization potential is not the most important value here, but what needs to be determined is whether a 0.1 eV difference in the ionization potential due to strain (as indicated in Fig. 4) could be responsible for the change in the SE signal as observed in the difference between neighbouring strained and relaxed $Ge_{0.25}Si_{0.75}$ layers in Fig. 2a–Fig. 2c.

Palmberg [24] has reported on extensive measurements of the work-function dependence of the SE yield from Ge (1 1 1) surfaces. Gradual reduction of the work function from 4.79 eV to 2.3 eV was achieved by deposition of a monolayer of Na. This Na monolayer left the BSE yield relatively unaffected but caused the SE yield to increase from 1.24 to 3.9 when using 1 keV incident electrons. An exponential dependence of the SE yield on the work function was found. By fitting a curve to Palmberg's data, a 3% increase in the SE yield can be determined when the work function is reduced from 4.79 eV to 4.69 eV. Using this data alone we can infer that the 0.1 eV decrease in the ionization potential due to strain in the $Ge_{0.25}Si_{0.75}$ layers (Fig. 4) should result in an increase in the SE signal by a few percent. The as-grown SE profiles from Fig. 2a–Fig. 2c show that the contrast between strained and unstrained $Ge_{0.25}Si_{0.75}$ layers differs by about 4%–7% which is representative of most of the SE profiles that were generated. These figures are a little higher that one might estimate from Palmberg's data (3%), but this is probably because adsorbates and oxide formation on the Si–$Ge_{0.25}Si_{0.75}$ cleavage surface have already lowered the ionization potential with the result that the further 0.1 eV strain-induced reduction in the ionization potential has a greater effect in percentage terms. This most likely accounts for the slightly higher than expected strain-induced contrast changes. A similar ionization potential-based estimate cannot be used for the SE contrast between the Si and $Ge_{0.25}Si_{0.75}$ layers because the BSE yields are higher in the $Ge_{0.25}Si_{0.75}$ layers resulting in increased SE2 generation by the exiting high-angle BSEs. A more rigorous analysis of SE emission from strained heterostructures should also include

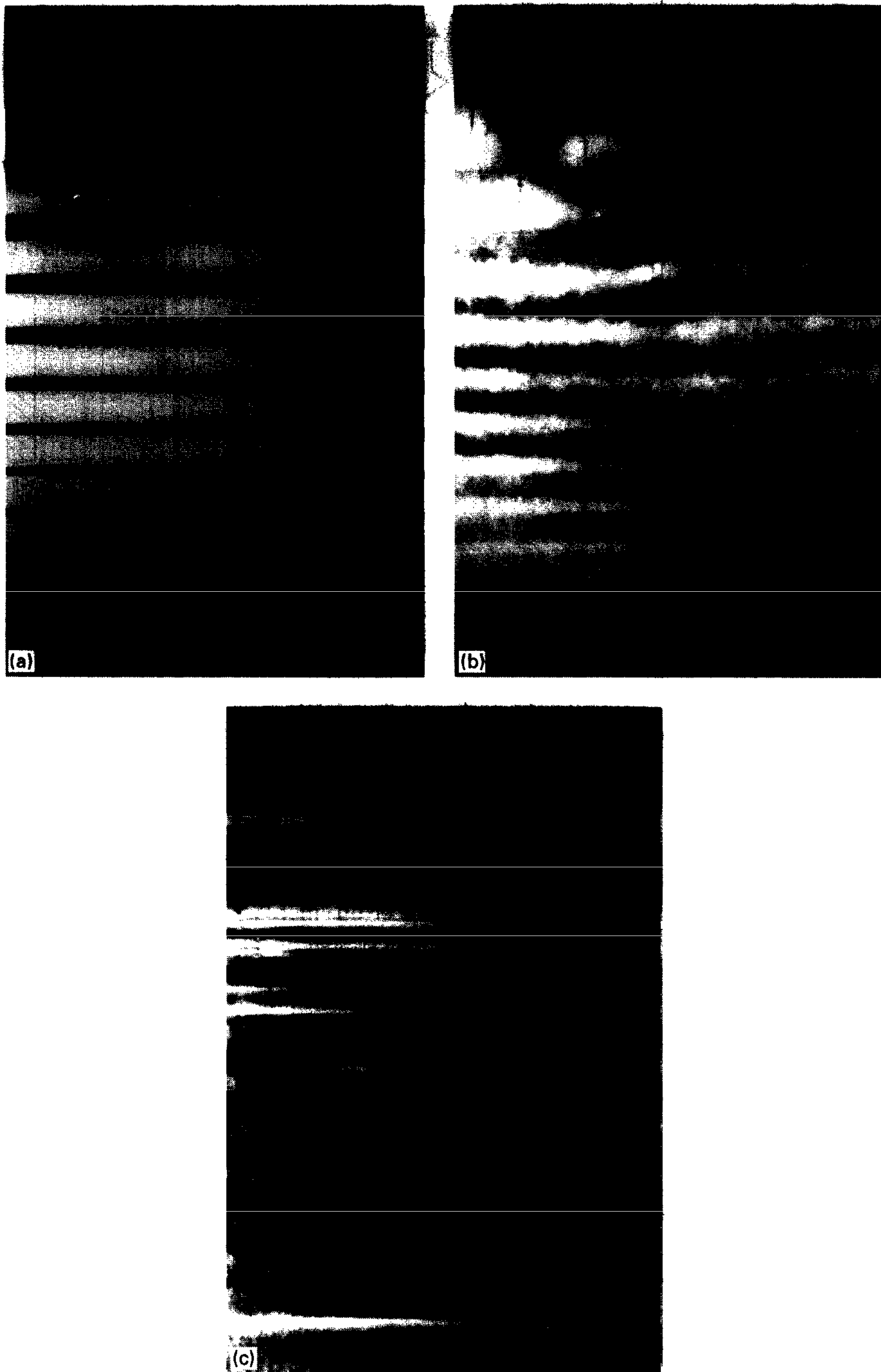

Fig. 3. (a) Cross-sectional bright-field TEM image of the as-grown structure using a weakly diffracting condition near the ⟨1 1 0⟩ zone-axis orientation. (b) Two-beam dark-field diffraction contrast image ($g = 2\,\bar{2}\,0$) of the as-grown structure. (c) Two-beam dark-field image ($g = 2\,\bar{2}\,0$) of the annealed structure (see text for details).

Fig. 4. Band alignments for a thin (strained) $Ge_{0.25}Si_{0.75}$ layer and a thick (relaxed) $Ge_{0.25}Si_{0.75}$ layer between unstrained Si layers. The valence band edge of strained $Ge_{0.25}Si_{0.75}$ lies 0.1 eV closer to the vacuum level than in the unstrained alloy. Strain causes a 0.1 eV reduction in the ionization potential resulting in enhanced SE emission from the strained region. SE excitation from surface states also contributes to the SE signal.

the effects of relaxation which will occur when cleaving normal to the layers [25].

4. Conclusions

In this paper we have presented measurements correlating compressive strain in $Ge_{0.25}Si_{0.75}$ layers with enhanced SE emission. This increase has been explained in terms of a small reduction in the ionization potential due to a 0.1 eV raising of the valence band edge in the strained layers. Although the difference in ionization potential between strained and unstrained $Ge_{0.25}Si_{0.75}$ layers is only a few percent, we have been able to detect this by optimizing the signal-to-noise ratio of the measurements through the use of the highly efficient SE detector [26] on the Hitachi S-4500 FE-SEM and effective image averaging techniques (as opposed to using single line-scan profiles).

Although work-function sensitive imaging is most effectively exploited through photoemission electron microscopy (PEEM) [27], this technique has a spatial resolution limit of around 200 nm. Here, we have shown that with SE imaging this resolution limit can be drastically improved into the range of a few nanometres. PEEM does not suffer from the effects of electron-beam-induced damage and also has a work-function resolution down to a few meV which will still make it most suitable for adsorbate sensitive imaging experiments. SE imaging also has the disadvantage that if the material under examination is not of uniform composition then it may be hard to deconvolve the effect of work function as opposed to other SE contrast mechanisms. However, where the experiment is not limited by the restrictions mentioned above, we have shown that SE imaging can offer work function or ionization potential sensitivity at nanometre-scale resolution.

Acknowledgements

We are grateful to R. Turan for preliminary work in this area. We would like to thank A. Howie for helpful comments and J.P. McCaffrey for preparing TEM samples. This work was funded through the Ontario Centre for Materials Research and Natural Sciences and the Engineering Research Council of Canada.

References

[1] K. Ogura, A. Ono, S. Franchi, P.G. Merli, A. Migliori, Proc. XIIth Int. Congr. Electr. Microsc. 1 (1990) 404.
[2] P.G. Merli, M. Nacucchi, Ultramicroscopy 50 (1993) 83.
[3] M.R. Castell, A. Howie, D.D. Perovic, D.A. Ritchie, A.C. Churchill, G.A.C. Jones, Phil. Mag. Lett. 67 (1993) 89.
[4] A.L. Bleloch, M.R. Castell, A. Howie, C.A. Walsh, Ultramicroscopy 54 (1994) 107.
[5] D.D. Perovic, M.R. Castell, A. Howie, C. Lavoie, T. Tiedje, J.S.W. Cole, Ultramicroscopy 58 (1995) 104.
[6] P.G. Merli, A. Migliori, M. Nacucchi, D. Govoni, G. Mattei, Ultramicroscopy 60 (1995) 229.
[7] D. Govoni, P.G. Merli, A. Migliori, M. Nacucchi, Microsc. Microanal. Microstruct. 6 (1995) 499.
[8] M.R. Castell, D.D. Perovic, A. Howie, D.A. Ritchie, C. Lavoie, T. Tiedje, Inst. Phys. Conf. Ser. 146 (1995) 281.
[9] P.G. Merli, A. Migliori, M. Nacucchi, M. Vittori Antisari, Ultramicroscopy 65 (1996) 23.
[10] D.D. Perovic, M.R. Castell, A. Howie, C. Lavoie, T. Tiedje, J.S.W. Cole, in: B. Jouffrey, C. Colliex (Eds.), Proc. 13th Int. Congr. on Electron Microscopy, vol. 1, Les Editions de Physique, Les Ulis, France, 1994, p. 91.
[11] C.P. Sealy, M.R. Castell, A.J. Wilkinson, P.R. Wilshaw, Inst. Phys. Conf. Ser. 146 (1995) 609.
[12] D. Venables, D.M. Maher, Inst. Phys. Conf. Ser. 146 (1995) 605.
[13] A. Howie, J. Microsc. 180 (1995) 192.
[14] D. Venables, D.M. Maher, J. Vac. Sci. Technol. B 14 (1996) 421.
[15] R. People, Phys. Rev. B 32 (1985) 1405.
[16] D.V. Lang, R. People, J.C. Bean, A.M. Sergent, Appl. Phys. Lett. 47 (1985) 1333.
[17] C.G. Van de Walle, R.M. Martin, Phys. Rev. B 34 (1986) 5621.
[18] D.D. Perovic, B. Bahierathan, H. Lafontaine, D.C. Houghton, D.W. McComb, Physica A, in press.
[19] H. Lafontaine et al., J. Vac. Sci. Technol. B 14 (1996) 1675.
[20] D.C. Houghton, D.D. Perovic, J.-M. Baribeau, G.C. Weatherly, J. Appl. Phys. 67 (1990) 1850.
[21] L. Reimer, in: Scanning Electron Microscopy, Springer Series in Optical Sciences, vol. 45, Springer, Berlin, 1985.
[22] L. Reimer, C. Tolkamp, Scanning 3 (1980) 35.
[23] A. Konkol, G.R. Booker, P.R. Wilshaw, Ultramicroscopy 58 (1995) 233.
[24] P.W. Palmberg, J. Appl. Phys. 38 (1967) 2137.
[25] M.M.J. Treacy, J.M. Gibson, A. Howie, Phil. Mag. A 51 (1985) 389.
[26] D.C. Joy, C.S. Joy, R.D. Bunn, Scanning, in press.
[27] H.H. Rotermund, Surf. Sci. 283 (1993) 87.